Received: 30 March 2021 | Revised: 30 June 2021 | Accepted: 2 July 2021

DOI: 10.1111/joa.13514

ORIGINAL PAPER

Journal of Anatomy ANATOMICAL SOCIETY WILEY

External surface anatomy of the postfolding human embryo: Computer-aided, three-dimensional reconstruction of printable digital specimens

Jon Jatsu Azkue

Department of Neurosciences, School of Medicine and Nursery, Universty of the Basque Country, UPV/EHU, Leioa, Bizkaia, Spain

Correspondence
Jon Jatsu Azkue, Department of Neurosciences, School of Medicine and Nursery, Universty of the Basque Country, UPV/EHU, Sarriena auzoa z/g, Leioa, Bizkaia 48940, Spain.
Email: jonjatsu.azkue@ehu.eus

Abstract

Opportunities for clinicians, researchers, and medical students to become acquainted with the three-dimensional (3D) anatomy of the human embryo have historically been limited. This work was aimed at creating a collection of digital, printable 3D surface models demonstrating major morphogenetic changes in the embryo's external anatomy, including typical features used for external staging. Twelve models were digitally reconstructed based on optical projection tomography, high-resolution episcopic microscopy and magnetic resonance imaging datasets of formalin-fixed specimens of embryos of developmental stages 12 through 23, that is, stages following longitudinal and transverse embryo folding. The reconstructed replica reproduced the external anatomy of the actual specimens in great detail, and the progress of development over stages was recognizable in a variety of external anatomical features and bodily structures, including the general layout and curvature of the body, the pharyngeal arches and cervical sinus, the physiological gut herniation, and external genitalia. In addition, surface anatomy features commonly used for embryo staging, such as distinct steps in the morphogenesis of facial primordia and limb buds, were also apparent. These digital replica, which are all provided for 3D visualization and printing, can serve as a novel resource for teaching and learning embryology and may contribute to a better appreciation of the human embryonic development.

KEYWORDS
3D graphics, developmental stages, human embryo, surface rendering

1 | INTRODUCTION

Embryology has long been an integral part of the medical school curriculum (Carlson, 2002; Drake et al., 2002). Not only is knowledge of embryonic development important in order to assimilate the spatial arrangement of organs in the body, but also proper understanding of normal human morphogenesis provides researchers and clinicians with a basis to interpret congenital anomalies, which are responsible for more than 25% of all neonatal deaths in the European Region (World Health Organization, 2008).

The human developmental stage system comprises 23 stages and is based on a morphological scheme that was first contrived by Mall (1914) and later advanced and completed by Streeter (1951) and O'Rahilly (1979). Ever since the early work by Mall (1914), who classed human embryos taking exclusively external characters as his guide, external morphology has remained the cornerstone of

embryo staging (Harkness & Baird, 1997; O'Rahilly, 1979; O'Rahilly & Müller, 1987, 2010). Moreover, criteria for *ex vivo* staging, such as the position of the limb buds or hands and feet, the bending of the elbow, or the curvature and general layout of the embryo's body, may be translated to the clinical setting for *in vivo*, sonographic estimation of at least some developmental stages (Parisi et al., 2019; Verwoerd-Dikkeboom et al., 2008). In addition, the morphogenesis of the cervicofacial region is best appreciated externally.

Knowledge of the anatomy of the human embryo has largely been built on the analysis of histological preparations, and opportunities for clinicians, researchers, and medical students to appreciate and become acquainted with the three-dimensional (3D) anatomy of actual embryos have historically been limited. The 3D anatomy of the embryo was classically approached by reconstructing wax models based on histological sections. Among the most notorious early embryo models stand the wax models made freehand by Wilhelm His and Adolf Ziegler, as well as those created by Gustav Jacob Born using wax plates (Born, 1883). New developments of the reconstruction methods (Heard, 1951, 1953) brought about the production of models with significantly improved accuracy over the early Ziegler models, such as those based on the Carnegie and Blechschmidt embryo collections. Wax models have now been replaced by commercial modern plastic versions. However, the Ziegler models are the basis of many of the teaching models that are commercially available and used today, despite limitations in accuracy and detail. Later on in the 20th century, the use of scanning electron microscopy allowed to visualize the 3D structure of the developing body in unprecedented detail (Fraser & Sato, 1989; Hendrix et al., 1985; Kluth et al., 1993; Männer et al., 1997; Steding, 2008; Toh & Ohmori, 1991), and only relatively recently has visualization of cross-sectional images of the human embryo become possible by using modern scanning technologies such as optical projection tomography (OPT; Kerwin et al., 2010), high-resolution episcopic microscopy (HREM; Weninger et al., 2006), episcopic fluorescence image capture (Yamada et al., 2010) and magnetic resonance imaging (MRI; Yamada et al., 2006, 2010). An important benefit of these imaging techniques is that they yield perfectly registered sectional images, which can be converted into volumetric datasets to be visualized in orthogonal or arbitrary planes and allow to generate high-quality 3D reconstructions. Models based on both modern imaging technologies (Kerwin et al., 2010; Weninger et al., 2006; Yamada et al., 2006, 2010) and conventional histology (de Bakker et al., 2016) have been incorporated into learning software applications and human embryo atlases, some of which can be accessed for visualization and download (http://hdbratlas.org; https://www.3dembryoatlas.com). However, 3D surface models that illustrate external anatomy over all sequential stages of development are not available.

Digital 3D models of the human embryo are highly desirable, not only due to the educational potential of anatomical 3D visualizations (Yammine & Violato, 2015) but also because digital models can be brought to a new dimension by printing physical, tangible anatomical replica using affordable desktop 3D printers. The 3D printing technology has already made an entrance to anatomy education (AbouHashem et al., 2015; Cai et al., 2019; Costello et al., 2014; McMenamin et al., 2014), and there is evidence showing that students using 3D printed resources learn anatomy better and with higher satisfaction (Lim et al., 2016; Ye et al., 2020). Ideally, digital 3D models of human embryos should feature all possible sequential stages of development in order to provide a comprehensive view of morphogenesis, they should be as accurate and realistic as possible, and should be made available for 3D visualization and printing. The goal of this work was to generate a collection of digital, printable 3D surface models demonstrating major developmental changes in the embryo's external anatomy over postfolding stages, including typical morphological features used for external staging. The study focused on human embryos of stages 12 through 23, that is, stages of development following longitudinal and transverse folding of the embryonic disk to form a cylindrical body.

2 | MATERIALS AND METHODS

2.1 | Human embryo specimens

Optical projection tomography, HREM and MRI datasets of formalin-fixed human embryos of Carnegie stages 12 through 23 were used. Details of original datasets are provided in Table 1. OPT images (stage 12 embryo) were generated from and distributed as part of the Human Developmental Biology Resource (HDBR, http://hdbratlas.org; Kerwin et al 2010) at the Institute of Genetic Medicine, Newcastle University (Newcastle upon Tyne, UK). HREM image stacks (stages 13–17, and 19) were generated by Dr. Tim Mohun (Heart Development Laboratory, Francis Crick Institute, London, UK; Geyer et al., 2009; Weninger et al., 2006), and made available at the Deciphering the Mechanisms of Developmental Disorders (DMDD) website (https://dmdd.org.uk/). Magnetic resonance imaging data of human embryo specimens of stages 18 and 20–23 were obtained from the Human Embryo Atlas hosted by the University of Pittsburgh School of Medicine (Dhanantwari et al., 2009; Yamada et al., 2010). These specimens had been scanned to produce data matrices of 256 x 192 x 192 to 512 x 512 x 512 dimensions with final resolutions of 30–117 μm/pixel (Yamada et al., 2010). The OPT and MRI specimens had already been staged in their original collections, whereas HREM datasets for this study were selected of those embryos that matched the appropriate criteria for the desired developmental stages.

2.2 | General workflow

All 3D reconstructions were performed using *ITK-SNAP Medical Image Segmentation Tool* software (v3.4.0; Yushkevich et al., 2006). Each reconstruction included a segmentation step, that is, delimitation of the boundaries of the target object, followed by generation of a surface polygon mesh representing those boundaries (Figure 1).

TABLE 1 Metadata of embryo datasets used for three-dimensional reconstructions

Carnegie stage	Imaging technique	Volumetric dimensions and resolution	Specimen ID and source
12	OPT	215 x 345 x 375, 8.2 μm/pixel	Cs12, HDBR
13	HREM	485 x 201 x 511, 2 μm/pixel	2917, DMDD
14	HREM	203 x 376 x 401, 2 μm/pixel	1238, DMDD
15	HREM	359 x 480 x 640, 3 μm/pixel	2102, DMDD
16	HREM	379 x 480 x 640, 3 μm/pixel	2098, DMDD
17	HREM	360 x 480 x 811, 3 μm/pixel	2096, DMDD
18	MRI	291 x 148 x 451, ca. 55 μm/pixel	17925, HEA
19	HREM	489 x 480 x 640, 3 μm/pixel	1653, DMDD
20	MRI	402 x 319 x 439, ca. 55 μm/pixel	20788, HEA
21	MRI	171 x 278 x 430, ca. 55 μm/pixel	14423, HEA
22	MRI	169 x 260 x 477, ca. 55 μm/pixel	21224, HEA
23	MRI	280 x 411 x 546, ca. 55 μm/pixel	17236, HEA

DMDD, Deciphering the Mechanisms of Developmental Disorders (https://dmdd.org.uk/); HDBR, Human Developmental Biology Resource (http://hdbratlas.org); HEA, Human Embryo Atlas (Dhanantwari et al., 2009; Yamada et al., 2010); HREM, high-resolution episcopic microscopy; MRI, magnetic resonance imaging; OPT, optical projection tomography.

The specimens' bodies were first segmented semiautomatically. The process starts by preselecting the target region whose boundaries would be ultimately found and delimited by active contours (see below). The preselection was done based on color properties of the tissue, namely by establishing a range of shades of gray for those *voxels* or volumetric image data that the system would consider as representing the embryo's body as opposed to those representing the background (e.g., black in MRI cross sections, or white in HREM images). This operation labeled a number of inner cavities with a color similar to the background as being outside the body (see below). Conversely, debris or tissue detached from the body was considered by the system as inside the body, based on color. Following color-based preselection, semiautomatic segmentation was completed by using the built-in active contour algorithm in ITK-SNAP (Kass et al., 1988). Active contours are computer-generated curves that propagate, through a series of iterations, until they reach the boundaries of the target object. This technique provides better control over the segmentation process by setting how many contours to use and where each contour should begin to propagate. For example, debris or detached fragments can be easily excluded from segmentation even if they have been set as target regions based on color. In addition, the active contour procedure allows to handle partial segmentations, based on different color parameters, whenever the dataset has regional variations in contrast or gray levels. As a result of this operation, a binary mask is created that distinguishes the voxels that will be held by the software as representing the embryo's body from those representing the background. At this stage, however, a number of closed cavities such as cardiac chambers, the lumen of the neural tube, and large blood vessels were labeled as located outside the body. These were segmented manually thereafter as belonging to the target object. Active contours also determined internal projections of the external space such as the oropharyngeal cavity and to varying extents also the lumen of the digestive tube, as empty spaces. Most of the digestive tube was segmented manually as belonging to the solid body, and thus only the foregut and the oropharyngeal cavity were kept labeled as empty spaces. The marching cubes algorithm (Lorensen & Cline, 1987) was then used to generate a 3D polygon mesh representing the boundaries of the segmented, target object. Polygon meshes were exported in Standard Tessellation Language (STL) format and postprocessed using Blender v2.76 software (Blender Foundation; www.blender.org). Model postprocessing for 3D visualization involved correction or restoration of damaged regions (see below), laplacian smoothing, remeshing, and polygon reduction. Laplacian smoothing removes noise locally by smoothing the position of a given vertex of the mesh based on information about its immediate neighbors, while preserving the general shape of the original model (Sorkine et al., 2004). Here, 20–25 iterations and a lambda factor of 0.2–0.3 were used for smoothing. Remeshing refers here to rebuilding the geometry of a mesh using more uniform polygons. The resulting meshes contained over a million vertices. In order to limit the file size of output models, the vertex count was reduced by ca. 90%, which resulted in about 20–30 MB files. The models were then scaled to the reported average size (10× greatest length) for each developmental stage (O'Rahilly & Müller, 2010) and made suitable for 3D printing by removing nonmanifold geometry and orienting polygon normals consistently.

2.3 | Specific reconstructions in individual models

Most original specimens reconstructed digitally in this study had some physical damage of minor character and were subject to restoration to varying degrees. The stage 12 specimen had a disrupted and partially collapsed fourth ventricle roof, which was lifted and restored (also discussed below). Remnants of the amniotic membrane

were removed and the umbilical vesicle was severed leaving only a short stalk. The lumen of a portion of the pharyngeal intestine was included in segmentation, caudal to the oropharyngeal cavity. The coelomic cavity was obliterated rostrally at the level of the pericardioperitoneal canals. In the stage 14 model, a collapsed fourth ventricle was lifted and restored, and the excess umbilical cord tissue

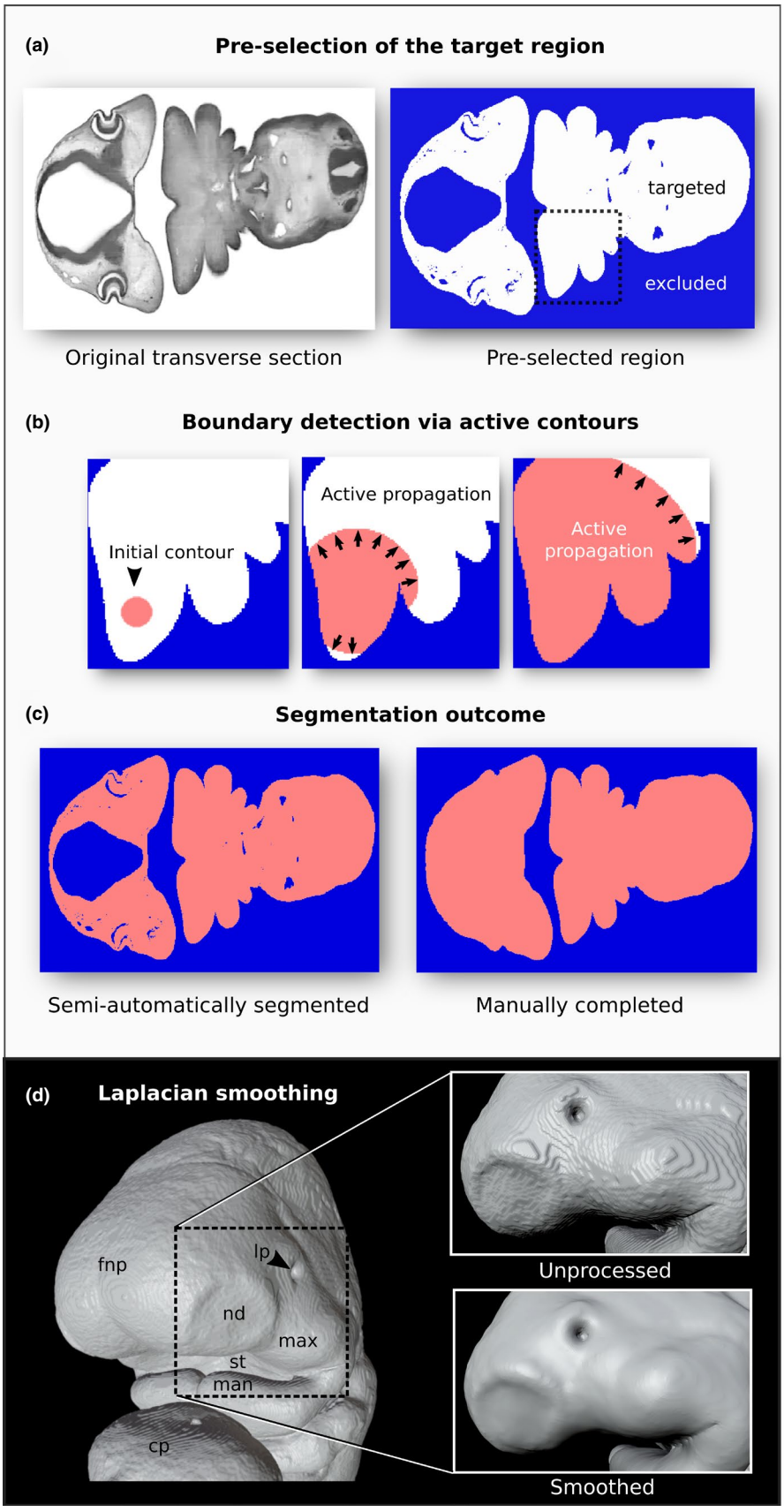

FIGURE 1 Key steps of the workflow for embryo reconstruction. (a) The region representing the body of the embryo is preselected (white filling) on cross-sectional images on the basis of gray color intensity against the background. The inset indicates the area enlarged in (b). (b) An active contour algorithm, which is based on propagation of one or more contours (red) until they reach the boundaries of the preselected region, is used to delimit the embryo's body. (c) The resulting segmented region (red) is corrected manually to label blood vessels and inner cavities, such as the neural tube, as belonging inside the body. The marching cubes algorithm is then used to generate a 3D polygon mesh representing the boundaries of the segmented object (shown in d). (d) Laplacian smoothing of the reconstructed surface. A model is shown prior to and following smoothing. fnp: frontonasal process; nd: nasal disc; max: maxillary process; man: mandibular process; st: stomodeum; lp: lens pit

was removed. In that of stage 15, the roof of the fourth ventricle was restored and minor damages were corrected at the root of the right lower limb bud and the dorsal curvature at the same approximate level. A small portion of the tail bud region and the umbilical cord were also restored. The stage 16 specimen showed a damaged left upper limb bud, which was restored by grafting a reproduction of the contralateral bud. Joined edges required additional smoothing to provide seamless transitions. In addition, the excess umbilical cord was cut off, a partially collapsed portion of the roof of the fourth ventricle was lifted, and a small damaged spot on the right mandibular process was corrected. In the stage 17 model, the excess umbilical cord was cut off, and the partially collapsed roof of the fourth ventricle was restored. This model was decapitated digitally and the oropharyngeal cavity was exposed by removing the overlying head region, in order to demonstrate additional editing possibilities. The stage 18 specimen had damaged hand and thigh regions, which were reconstructed based on the contralateral limbs. Wrinkles, holes, and partially collapsed spots in the fourth ventricle region were also corrected. The stage 19 model underwent a restoration of the skin overlying the liver. The models corresponding to specimens of stages 20 through 23 underwent smoothing and correction of wrinkled or damaged areas of the skin.

The roof of the fourth ventricle was restored digitally in several models, as indicated above. Partial collapse of the rhombencephalic region is rather common in specimens ranging from stage 12 to about stage 18 or even beyond, due to extreme thinness of both the area membranacea and the overlying cutaneous layer. In intact embryos, this is a flattened or slightly convex surface, as shown previously in whole specimens and described in profile reconstructions (Müller & O'Rahilly, 1980, 1987; O'Rahilly & Müller, 1987). Since the roof of the fourth ventricle does not contain any structure of interest from an external anatomy viewpoint, 3D reconstructions did not require specific criteria other than consistency with the normal appearance of the region in intact specimens.

3 | RESULTS

Surface polygon meshes representing the external anatomy of 12 human embryo specimens of stages 12 through 23 were reconstructed and prepared for 3D visualization and printing. Previously published major features of the external surface morphology of postfolding human embryos are summarized in Table 2 for general reference, and a detailed account of the external morphology of the reconstructed models is provided below.

3.1 | Stage 12 model

The dorsal curvature of the body exhibited a smooth C-shaped convexity, due to the prominence of the spinal cord, the somites and the surrounding mesoblast (Figure 2a). The caudal neuropore, which can be open in earlier specimens of this stage, was however closed in the present specimen.

Three pharyngeal arches were visible, which were starting to become subdivided into dorsal and ventral sections. The otocyst was closed, and a slight opening pore that is usually still found in some specimens before detachment of the otic vesicle was not recognizable in the one reconstructed here.

Although there was no conspicuous upper limb bud, a slight bulge representing the primordium of the upper limb could be outlined on each side opposite somites 8–10, which merged caudally with the ventrolateral unsegmented strip of mesoblast on the body wall underlying the membral ectodermal ring. No analogous primordia corresponding to the lower limb were present.

The heart bulged outward as a smooth and voluminous prominence caudal to the pharyngeal region. An umbilical cord was taking form at the ventral aspect of the embryo. The umbilical vesicle was narrowing down, as was the opening of the coelomic cavity. The umbilical vessels traversed this opening in a separate compartment.

3.2 | Stage 13 model

The dorsum of the body still presented a C-shaped curvature, largely determined by the external contour of the neural tube (Figure 2b). A salient frontonasal prominence and a tail bud were present at the cranial and caudal ends of the body, respectively. Maxillary and mandibular processes could be distinguished as divisions of the first arch. Four pharyngeal arches were present, and caudal to the fourth arch was the depressed triangular area corresponding to the floor of the cervical sinus. The otocyst was completely closed off from the surface and no remnants of a connecting pore were present. The lens discs were distinguishable as two subtle convexities lateral to the frontonasal prominence, with no visible indentations. Both upper and lower limb buds were distinguishable. The upper limb buds exhibited distinct ridges, in contrast with the less developed lower limb buds. The heart exhibited a smooth surface and no indentations demarcating the underlying cardiac chambers. The external opening of the coelomic cavity was virtually obliterated.

TABLE 2 Major surface anatomical features of postfolding staged embryos

Stage	Greatest length (mean [min–max])	Days postfertilization	Major external anatomical features
12	3.9 (3–5.4)	29–31	Caudal neuropore closes. 3–4 pharyngeal bars. Upper limb buds appearing.
13	4.96 (3.9–6)	30–33	Four limb buds. Lens disc appears. Otic vesicle closed.
14	6.5 (4.9–8.2)	33–35	Lens pit present.
15	7.8 (6–11)	35–37	Lens vesicle internalized. Nasal pit appears. Primordium of antitragus. Hand plate formed. Trunk relatively wider.
16	9.6 (7–12.2)	37–40	Nasal pit displaced ventrally. Auricular hillocks beginning. Foot plate formed.
17	12.2 (10–14.5)	39–42	Head relatively larger. Trunk straightens. Nasofrontal groove distinct. Auricular hillocks distinct. Finger rays present.
18	14.9 (11.7–17.2)	42–45	Body more cuboidal. Elbow region and toe rays appearing. Eyelid folds may begin. Tip of nose distinct.
19	18.2 (15.5–21.5)	45–47	Trunk elongating and straightening.
20	20.7 (18–23)	47–50	Upper limbs longer and bent at elbows.
21	22.9 (20–26.4)	49–52	Fingers longer. Hands approach each other. Feet approach one another.
22	25.5 (23.4–27.5)	52–55	Eyelid and external ear more developed.
23	28.8 (23–32.2)	53–58	Head more rounded. Limbs longer and more developed.

Morphological highlights are adapted from O'Rahilly and Müller (1987), whereas chronology and embryo dimensions conform to O'Rahilly and Müller (2010).

3.3 | Stage 14 model

The dorsal curvature of the body was determined by that of the central nervous system and showed slight irregularities at cervicooccipital levels (Figure 2c). Thus, a cervical bend was apparent in the body surface, consistent with the cervical flexure of the neural tube. In addition, the so-called Nackengrube of His (His, 1882), that is, a subtle depression in the dorsal contour of the body opposite sclerotomes 5 and 6, which is commonly observed in embryos this age (O'Rahilly & Müller, 1987), was also distinguishable in the reconstructed model. In the head region, the first and second pharyngeal arches were sizable and prominent, whereas the third and the fourth arches were relatively small and partly concealed along with the depression of the cervical sinus. The ventral section of the second pharyngeal arch was further subdivided into dorsal and ventral segments. An open lens pit resulting from invagination of the lens disc was distinguishable. The nasal disc was largely flat and surrounded by slightly elevated medial and lateral nasal prominences.

The upper limb buds were rounded projecting appendages curving ventrally and tapering toward the tip. The lower limb buds were smaller in size and less ventrally curved. There was a slightly bulging band related to the abdominal musculature extending from the upper bud to the lower one.

3.4 | Stage 15 model

The dorsal curvature of the body was still slightly distorted by a cervical bend, which was however somewhat less pronounced than at the preceding stage, as well as by the presence of the Nackengrube more caudally (Figure 2d). From the dorsal view, the trunk region appeared wider than that of the preceding stage, due to the growth of the spinal ganglia and the muscular plates of the

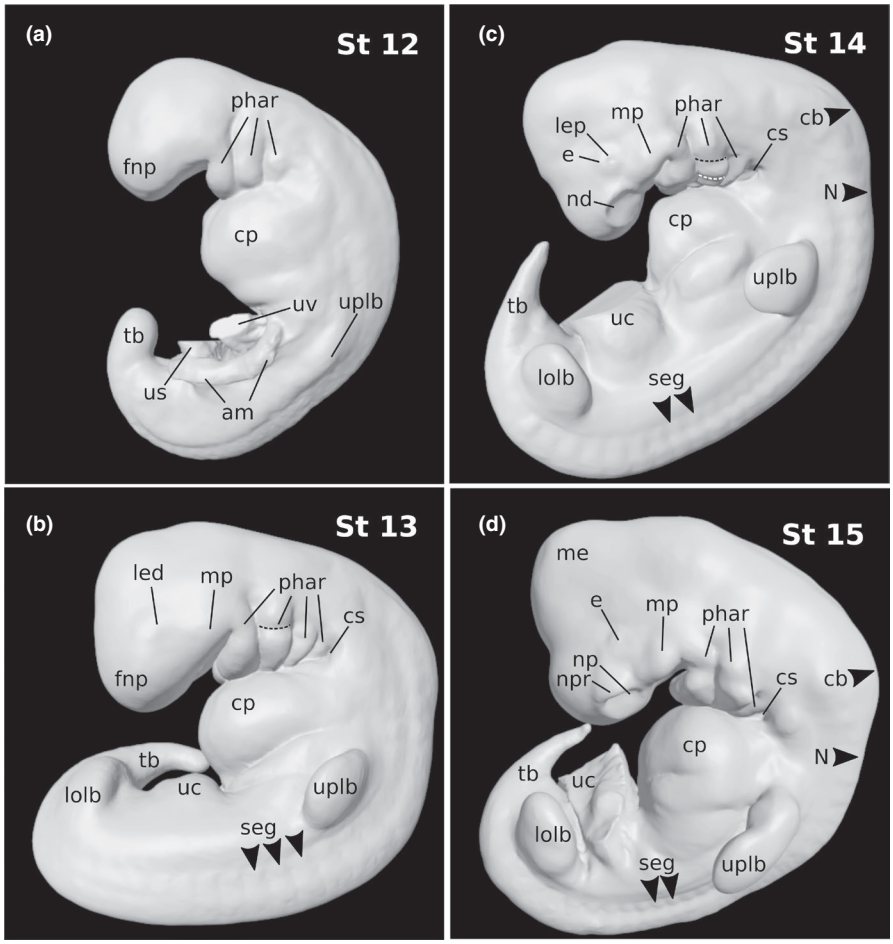

FIGURE 2 Three-dimensional models of human embryo specimens of stages 12 through 15. The external curvature of the body is largely determined by the morphology of the underlying neural tube. Up to four pharyngeal arches appear, with the third and fourth eventually beginning to recede from the surface. The upper and lower limb buds first appear at stages 12 (a) and 13 (b) respectively. Nasal discs first appear at stage 14 (c) and exhibit a central depression or nasal pit by stage 15 (d). The external opening of the coelomic cavity, which is still present at stage 12, is virtually already closed by stage 13. uplb: upper limb bud; lolb: lower limb bud; phar: pharyngeal arches (dashed lines indicate ongoing subdivisions); cp: cardiac prominence; fnp: frontonasal prominence; tb: tail bud; uv: umbilical vesicle; uc: umbilical cord; us: umbilical stalk; am: amniotic membrane (cut edge); cs: cervical sinus; mp: maxillary process; seg: segmented axial mesoderm; N: Nackengrube of His; nd: nasal disk; led: lens disk; lep: lens pit; me: mesencephalic prominence; npr: nasal process; np: nasal pit; e: eye

dorsum. In addition, the cervicooccipital region was wider than the lumbosacral section because of the rostrocaudal gradient in growth. The somites and underlying spinal ganglia produced distinctive elevations of the surface ectoderm throughout the spine region.

Three pharyngeal arches were distinguishable. The mandibular process was more prominent than the maxillary process. The lens pits were closed to give rise to lens vesicles and had thus disappeared from the surface. A nasal pit began to appear in the form of an oval depression within the nasal disc, due to the relatively greater growth of the surrounding tissues. The lateral nasal prominence was more pronounced than the medial process.

The upper limb bud became regionally subdivided into a distal segment comprising the hand plate and proximal forearm, and a proximal segment including the arm and shoulder regions. The relatively less developed lower limb bud began to subdivide into a rounded proximal portion and a more tapering distal one.

3.5 | Stage 16 model

The dorsal curvature of the body was smoother than in the preceding stage. Spinal ganglia were evident on the surface throughout the whole length of the trunk (Figure 3a). Elevations produced by longitudinally segmented mesoderm were present in the caudal part of the body.

The nasal areas were still separate. However, they were displaced medially as a consequence of the widening of the head, and the floor of the nasal pit was only partially visible from a lateral view, covered in part by an overhanging lateral nasal prominence.

The ventral sectors of the first and second pharyngeal arches were displaced medially and became only partially visible from a lateral view. The second arch appeared enlarged due to the formation of the precursors of the auricular hillocks. The third pharyngeal arch was receding from the surface within a small cervical sinus, largely covered over by the second arch. The maxillary fields bulged as

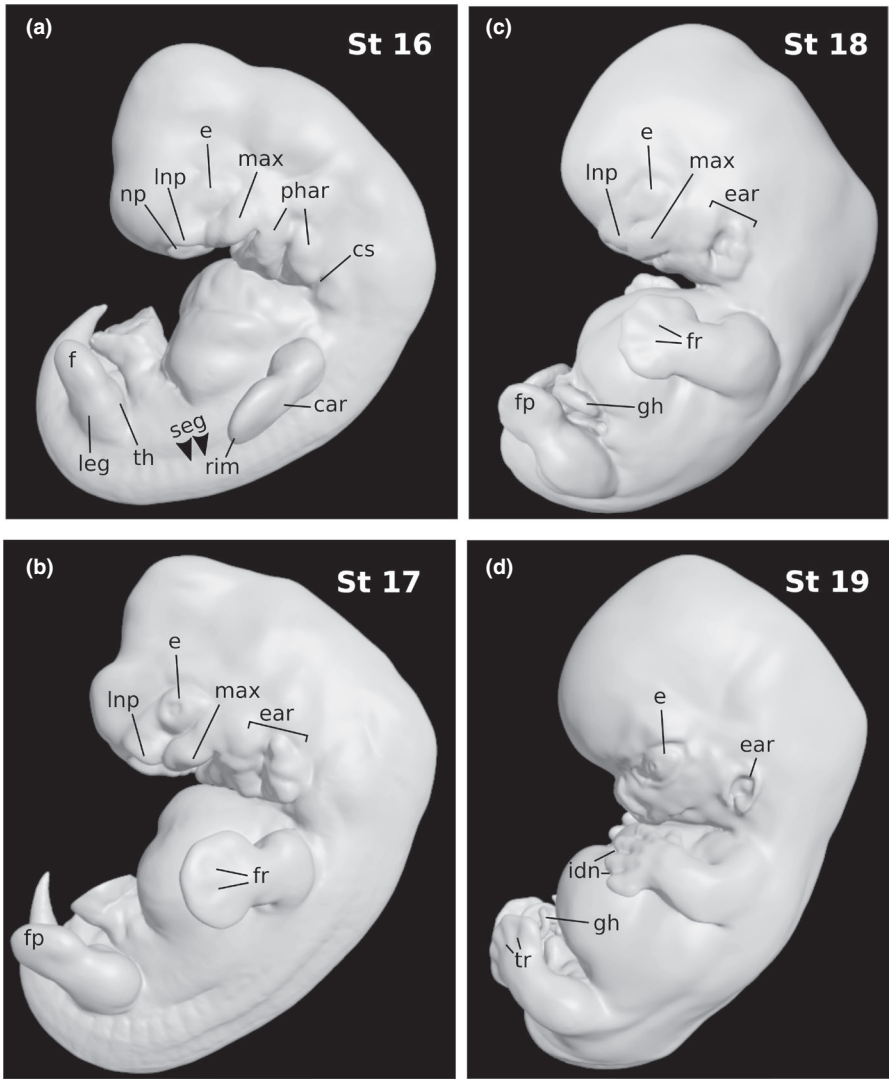

FIGURE 3 Three-dimensional models of human embryo specimens of stages 16 through 19. The dorsal curvature of the body is becoming smoother and the tail bud becomes relative small. Elevations produced by the underlying spinal ganglia and segmented mesoderm are hardly distinguishable rostrally at stages 16 (a) and 17 (b), and gradually disappear by stages 18 (c) and 19 (d). The third pharyngeal arch recedes from the surface and auricular hillocks start to form an external ear. The nasal pits displace ventrally and medial nasal prominences fuse in the median plane. Finger rays and interdigital notches appear in the hand plates, and toe rays are distinguishable by stage 19 (d). The physiological gut herniation is already evident by stage 18 (c). seg: elevations by underlying segmented mesoderm; e: eye; phar: pharyngeal arches; cs: cervical sinus; max: maxillary process; np: nasal pit; lnp: lateral nasal prominence; car: carpal region; rim: rim of hand plate; th: thigh region; leg: leg region; f: foot region; fp: foot plate; fr: finger rays; tr: toe rays; ear: auricular hillocks and emerging ear; gh: physiological gut herniation; idn: interdigital notches

widely separated prominent ridges in close proximity to the nasal prominences.

The upper limb bud featured a hand region comprising a central carpal region surrounded by a thick rim soon to give rise to the digits. The lower limb bud was starting to become subdivided into thigh, leg, and foot regions.

3.6 | Stage 17 model

The trunk had become straighter and began to show the lumbar flexure area. The head and neck region was larger in proportion than at preceding stages due to the growth of the brain (Figure 3b). The lumbosacral region remained slim relative to the head and the thorax, which had become wider. The spinal ganglia at the cervical and upper thoracic regions were hardly distinguishable on account of the increase in superficial embryonic connective tissue at these levels. Ectodermal elevations originated by longitudinally segmented mesoderm were most apparent in the lumbar and sacral regions, and less so at lower thoracic levels.

The third pharyngeal arch had completely disappeared from the surface. The six auricular hillocks separated by the hyomandibular groove could be distinguished, three on the first pharyngeal arch and three on the second arch. The ones on the mandibular arch, which were to give rise to the tragus and the crus helicis, were less bulging.

The nasal pit had shifted further medially and was no longer visible from a lateral view. It was further depressed as a flattened pocket to form the nasal sac, close to the roof of the mouth cavity. The medial nasal processes were divided into cranial and caudal sectors, the latter of which were destined to form the premaxilla.

The upper limb bud exhibited emerging finger rays. The tips of individual digits were not clearly distinguishable, indicating that the reconstructed specimen did not belong to the most advanced members of the group. The lower limb bud had a rounded digital area distal to the tarsal region and leg.

Although the physiological gut herniation had already begun, the herniated midgut loop was contained within the umbilical cord and was not apparent on the surface of the model. A decapitated version of this specimen and a preparation showing the anatomy of the floor of the oropharyngeal cavity, which were created by editing the model digitally, are shown on a separate plate (Figure 4).

3.7 | Stage 18 model

From a lateral view, the external contour of the body had begun to adopt a cuboidal form (Figure 3c). Somitic elevations were hardly distinguishable. The auricular hillocks were merging around the auditory cleft. The two dorsal hillocks on the first pharyngeal arch were merging to form the crus helicis, whereas the ventral one persisted to become the tragus. The nostrils and nasal wings were readily distinguished, and the medial nasal processes were beginning to fuse in the median plane. The area where the bridge of the nose was beginning to grow could be recognized from a lateral view. No eyelid folds were present.

The limbs had grown longer. In the upper limb bud, the hands had distinct finger rays and the tips of individual digits had begun to become distinguishable, separated by interdigital notches. The elbow region was discernible. In the lower limb bud, neither toe rays nor interdigital notches could be identified yet. The physiological gut herniation was evident.

3.8 | Stage 19 model

The trunk had begun to straighten slightly (Figure 3d). Ear hillocks had largely fused, although the ventralmost hillock on the second arch, which was to form the antitragus, was distinctly identifiable. Medial nasal prominences had fused to form the philtrum and septal elements of the nose. The nasofrontal angle could be seen clearly from a lateral view. Eyelid folds were beginning to become eyelids.

The four limbs were largely projected forward. In the upper limb bud, finger rays were distinctly visible and interdigital notches were more apparent than in the preceding stage. In the lower limb bud, toe rays were prominent but no interdigital notches were yet present.

3.9 | Stage 20 model

The upper limbs had elongated and were bent at the elbows to some extent (Figure 5a). The hands were undergoing pronation, and finger tips were clearly separated. Interdigital notches were present in the lower limb bud.

3.10 | Stage 21 model

The hands were slightly flexed over the cardiac eminence and fairly close to one another (Figure 5b). The feet were nearly touching each other in the median plane.

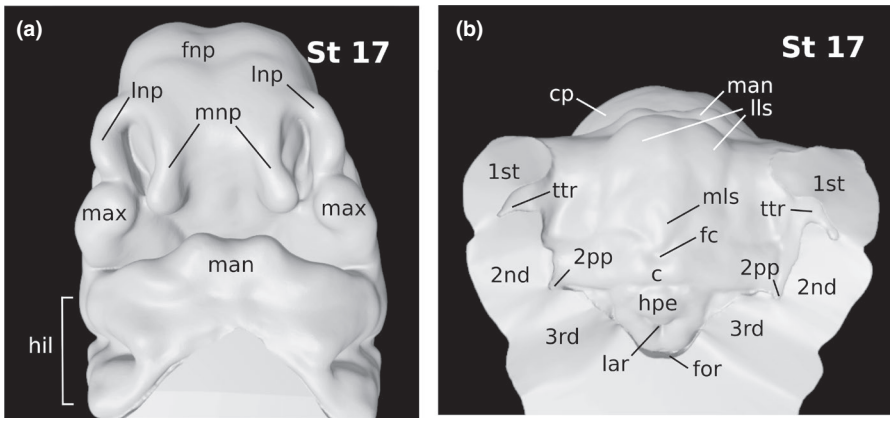

FIGURE 4 Digital dissection of the stage 17 specimen model. Ventral view of the facial region after digital decapitation of the stage 17 model (a), and upper view of the oral cavity and pharyngeal gut of the same model after digital opening and removal of the roof of the cavity (b). fnp: frontonasal prominence; mnp: medial nasal process; lnp: lateral nasal process; max: maxillary process; man: mandible; hil: auricular hillocks; 1st: first pharyngeal arch; 2nd: second pharyngeal arch; 3rd: third pharyngeal arch; for: foregut; lar: laryngeal orifice; mls: medial lingual swellings; lls: lateral lingual swellings; fc: foramen caecum of tongue; c: copula; hpe: hypopharyngeal eminence; cp: cardiac prominence; ttr: tubotympanic recess; 2pp: second pharyngeal pouch

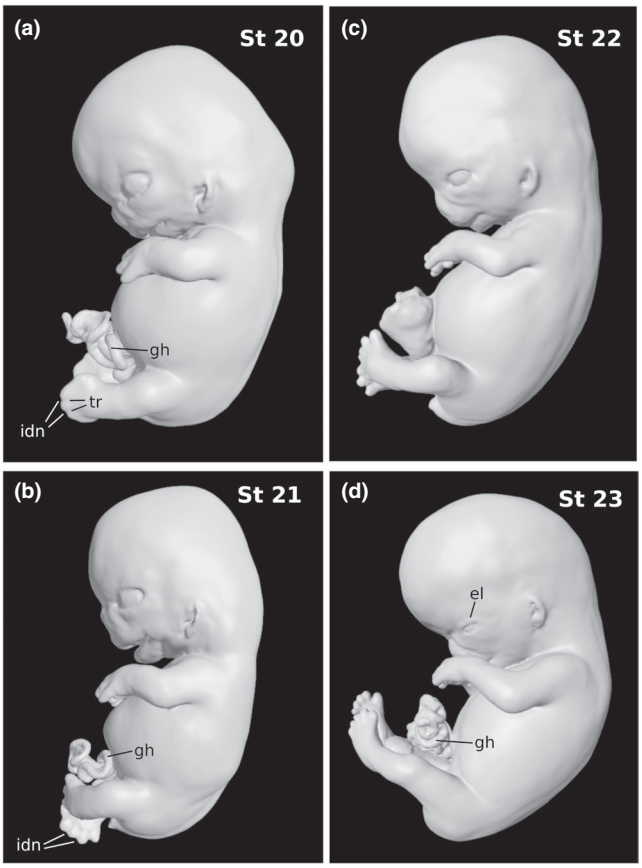

FIGURE 5 Three-dimensional models of human embryo specimens of stages 20 through 23. By the end of the embryonic period (d), the head is becoming more rounded, and the general shape of the body is closer to that of a fetus. Subdivision of the upper limb bud into shoulder, arm, forearm, and hand regions can be clearly observed. The hands are bending at the wrist with a slight pronation, and approximate each other. The finger tips are separating. At stages 22 (c) and 23 (d), the forearms and hands ascend toward the face. Feet are projected medially and become closer to each other. Interdigital notches appear and toes eventually separate. The eyelids cover more of the eye surface and start to close gradually. The physiological gut herniation is still in progress. gh: physiological gut herniation; el: eyelid; idn: interdigital notches; tr: roe rays

3.11 | Stage 22 model

The eyelids were covering more of the eye surface (Figure 5c). The hands projected further medially, in pronation and slightly flexed at the wrist, and finger tips of one hand were overlapping those of the other. Feet were further projected medially and toes were nearly in contact with the contralateral ones.

3.12 | Stage 23 model

The eyelids were closing gradually and covering still more of the eye surface (Figure 5d). The head was largely rounded, and the cervical region and trunk were closer in shape to that of a fetus.

The limbs had elongated and subdivisions could be clearly distinguished. The forearms and hands ascended toward the face. The carpometacarpal region had lengthened and adopted a more natural shape. The physiological gut herniation was still in progress. The external genitalia were not sufficiently developed to determine the specimen's sex.

4 | DISCUSSION

4.1 | Technical aspects

The accuracy and the level of detail of a polygon mesh reconstructed by segmentation of cross-sectional images are heavily dependent on the resolution and correct registration of sections, as well as on the polygon count of the output mesh. In the present context, image registration refers to the alignment of multiple sectional images into one coordinate system. Reconstructions of human embryo specimens from histological preparations of the Carnegie Collection have been undertaken previously (de Bakker et al., 2016; see also *The Virtual Human Embryo* at https://www.ehd.org/virtual-human-embryo). Unfortunately, this approach is not devoid of limitations related to structural distortion. Although computer techniques are now available to improve registration of digitized histological sections (Pichat et al., 2018), distortion is still introduced by uneven sectioning, deformation during mounting, and further processing of the tissue (Turner, 1920; Yamada et al., 2007), and the resulting reconstructions may require extensive smoothing of surface irregularities with a loss of morphological detail and realistic appearance. In contrast, sectional images derived from computer-based image acquisition technologies, such as OPT, MRI, and HREM imaging, yield perfectly aligned sectional image data and thus support more accurate reconstructions (Kerwin et al., 2010; Weninger et al., 2006; Yamada et al., 2007). There were differences among the models in this study as to the quality of reconstruction and morphological detail, and best results in this respect were obtained from high resolution (2–3 μm/pixel) HREM data. The level of detail exhibited by a number of anatomical structures of the corresponding models (stages 13 through 17), including for example the pharyngeal arches, nasal and maxillary processes, or the characteristic surface elevations produced in the dorsum by the underlying dorsal root ganglia and segmented mesenchyme, was comparable to that provided by scanning electron microscopy (Steding, 2008). On the other hand, segmentation of eyefolds and natural orifices such as the nostrils and the external acoustic canal from MRI data of advanced embryos was difficult and resulted in comparatively less morphological detail.

The polygon count of a model, that is, the total number of polygons that the model's mesh is composed of, is a prevalent issue in 3D reconstruction and 3D rendering. A model with a higher polygon count can retain richer morphological detail but will also demand higher computational effort to process and visualize. Conversely, reducing the number of polygons helps process a model more

efficiently but can compromise detail. In this study, preliminary attempts showed that heavy decimation of the meshes compromised the level of detail of small or subtle external features such as the lens pit, finger or toe rays, and subdivisions of pharyngeal arches. These were used as a reference during the process of polygon reduction, with the primary premise of preserving realistic appearance.

There is limited information available on the original embryos for comparison with the reconstructed models. Whole specimens of stage 12 (OPT) and stages 13–17, and 19 (HREM), which are available for viewing as movie clips at the HDBR and DMDD web sites, are all volume renders that can hardly been directly compared with surface reconstructions. A volume render is a two-dimensional projection simulated by computing the absorption and emission of light rays cast through a 3D dataset of voxels, and can thus show both superficial and internal organs by assigning convenient levels of opacity to voxels, whereas surface models are not actually composed of voxels but by an empty polygon mesh that represents the external boundaries of an object. Volume renders and surface renderings of polygon meshes are different types of data and imaging techniques altogether, and therefore direct comparisons are not reliable and in many cases not even possible. For example, the volume-rendered specimen HREM 1238 available at the DMDD web site exhibits both a lens pit and the underlying evaginated optic cup, due to semitransparency assigned to the voxels representing the skin, whereas a surface model will only show an invaginated pit as an indentation on the skin (Figure 2c). On the other hand, the morphology of the lens pit is hardly distinguishable in the volume-rendered specimen, due to translucency of the voxels representing the skin. The intracraneal venous plexus and a semi-transparent umbilical cord that are visible in the volume-rendered 1238 specimen cannot be surface rendered unless they have been reconstructed as separate polygon meshes. In addition, the stage 12 specimen available for viewing at the HDBR atlas web site exhibits a neural tube through the translucent and hardly distinguishable skin, in sharp contrast with a surface model such as the one reconstructed in this work, where the skin, but not the neural tube, is visible (Figure 2a).

4.2 | Surface anatomy for external staging

The external anatomy of the embryo provides essential information to assess developmental progress (Table 2). Some individual external features described previously as characteristic of each stage were of limited use for precise staging. For example, three or four pharyngeal arches have been described as being present already by stage 12 (O'Rahilly & Müller, 1987). The stage 12 specimen in the present study showed only three arches (Figure 2), which was unlikely due to immaturity of the specimen, as indicated by the already closed caudal neuropore, whereas the fourth arch was only present here at stages 13 and 14 in the depression of the cervical sinus (Figure 2), only to be eventually concealed by the third arch and sink in at stage 15. In addition, the antitragus is described as beginning to form at stage 15, whereas the auricular hillocks, that is, the precursor structures of the ear, are first mentioned at stage 16 (O'Rahilly & Müller, 1987). In this respect, it appears more informative to refer to the ventralmost segment of the second pharyngeal arch (stages 14–15) as the precursor of the sixth auricular hillock (stage 17), which will later give rise to the antitragus. Other external morphological features, yet easily recognizable in reconstructed embryos, appear to be of limited use, individually, for staging purposes. These include, for example, the head proportions, the dorsal curvature of the back, or the rostrocaudal gradient in dorsal width. The curvature of the embryo has been used as a morphological reference for ultrasonic embryo staging (Parisi et al., 2019). In the present models, however, a lateral view of the present reconstructed embryos fails to reveal any particularity of the dorsal curvature as distinctly specific to a given stage. Despite the above, a few other external morphological characteristics were remarkably stage-specific. The presence of the lens pit, that is, the narrow opening of the invaginating lens plate to the surface, was coherent with internal features of stage 14, such as the ventral growth of the primordium of the cochlear bud in the otic vesicle, the first appearance of the nephrogenic cup, and the growth of lung buds dorsalad to embrace the oesophagus laterally (Ludwig & Landman, 2005; Müller & O'Rahilly, 1988; O'Rahilly & Müller, 1987). In addition, the formation of the nasal pit and its later displacement toward the median plane in the present specimens of stages 15 and 16 were synchronous with typical internal and external developmental features of the respective groups (O'Rahilly & Müller, 1984a,b, 1987, 1994). Thus, closed lens vesicles, emerging lobar subdivisions in the lung buds, and a clear subdivision of the upper limb buds into proximal and distal segments were present in the former, whereas the stage 16 specimen exhibited a third pharyngeal arch already starting to recede from the surface, a reniform metanephros still in a sacral position, and a subdivided lower limb bud into proximal and distal segments. Moreover, anatomical changes undergone by the developing limbs were also quite specifically related to standard stages. From the first appearance of the upper limb rudiments at stage 12 up to limb elongation and elbow bending at stage 20, each intermediate stage was characterized in the present specimens by a specific morphogenic status (O'Rahilly & Müller, 1987), including the sequential appearance of upper and lower limb buds, the development of hand and foot plates, and the formation of finger and toe rays. The bending of the elbow region as identified *intra utero* by ultrasonographic exploration of the conceptus has been used by Verwoerd-Dikkeboom et al., (2008) to distinguish stage 19 from stage 20, and Blaas et al., (1998) have succeeded in distinctly identifying the hands in an embryo of crown-rump length of 14.8 mm, which may correspond to stage 18 (Olivier & Pineou, 1961; O'Rahilly, 1979). In addition, a previous study has successfully staged human embryos based on the external development of the limb buds (Harkness & Baird, 1997). These observations are thus in agreement with the external morphology of the models reconstructed in this study, and collectively lend support to the validity of external staging.

4.3 | Three-dimensional visualization and printing of human embryos

Three-dimensional models have long been essential for teaching anatomy. Nowadays, digital 3D models can be viewed in most electronic devices, and there is a body of evidence supporting the efficacy of 3D visualizations for acquisition of both spatial and factual anatomical knowledge (Yammine & Violato, 2015), including understanding of the complexities of developmental anatomy (Marsh et al., 2008; Tait et al., 2020). For a collection of digital embryo models to have a high educational value, the models should represent all possible sequential stages of development in an accurate and realistic manner. This study addresses this issue differently from previous approaches. Yamada et al., (2018) reconstructed embryo models from X-ray computed tomography and MRI data, which were then extensively refined and added morphological detail digitally to generate quasi-idealized models for use as computer-based self-learning materials. Here, in contrast, reconstructed models were postprocessed less extensively in order to retain the original specimens' natural appearance. Another approach was taken by de Bakker et al., (2016), who created a comprehensive human embryo atlas based on reconstructions of embryos of a range of stages from conventional histology. Importantly, those models exhibit both external and internal anatomy and are all available for download and 3D visualization from the Internet (https://www.3dembryoatlas.com). In this work, models were reconstructed from computer-based embryo imaging data, which yield perfect registration and thus provide ideal volumetric data for 3D reconstructions. In addition, volume renders of whole embryos generated from OPT and HREM imaging data and surface models of several organ systems can be viewed revolving around the vertical axis in movie clips available at the Human Development Biology Resource project web-site (http://hdbratlas.org). User interactivity other than stop-and-go is however unavailable. This issue was addressed here by embedding 3D models in PDF, which allows visualization with a number of rendering and lighting options, as well as manipulation of the models by rotation, displacement, and zooming in/out as desired. These are all considered as desirable general functionalities for 3D anatomy education (Zilverschoon et al., 2019).

Additive manufacturing or 3D printing technology has advanced enormously and has become widely accessible for construction of physical replicas of digital models. Printed physical models are now being increasingly used for anatomy education (AbouHashem et al., 2015; Cai et al., 2019; Costello et al., 2014; McMenamin et al., 2014), and recent evidence shows that students using 3D printed resources learn anatomy better (Lim et al., 2016; Ye et al., 2020). There is to date little documentation on the use of 3D printed material for teaching human embryonic and prenatal anatomy (Jarvis et al., 2016; Young et al., 2019). This study provides, for the first time, 3D printable models reconstructed from specimens of consecutive stages of development, which make the microscopic anatomy of the embryo tangible to students, researchers, and clinicians. Accurate and realistic physical models are particularly important for learning human embryology, since whole specimens are hardly available for manipulation and study, and commercially available teaching models show limited anatomical detail and generally fail to depict developmental stages. It is noteworthy that the present models can be used not only directly for 3D visualization and printing, but can also be rescaled or edited to pursue specific learning objectives. For example, the morphogenesis of the face is best appreciated in decapitated models (Figure 4), not unlike in actual specimens. In addition, models of stages 12 through 17 can be further dissected to expose the structure of the oropharyngeal cavity in order to appreciate the development of the pharyngeal pouches, tongue, and palate (Figure 4).

4.4 | Limitations and future work

All original embryo specimens were fixed in formalin, which might introduce some distortion in the volumes of reconstructed models. Although the effect on body proportions and general morphology of reconstructed models is negligible, these may not well bell suited for morphometric analysis.

This study included human embryo specimens of postfolding stages only, which was due to limited availability of prefolding specimen data other than conventional histology. On the other hand, although relevant external anatomy for staging was apparent in the present series, only one specimen was reconstructed per stage and thus the study does not describe normal variability. Studies are thus awaited to address this issue using appropriate sample sizes. Finally, future additions should include reconstructions of internal structures and organic systems during both normal and abnormal development, in order to maximize the educational value of 3D models of the human embryo.

ACKNOWLEDGMENTS

The author is deeply indebted to Dr. Tim Mahoun (Heart Development Laboratory, Francis Crick Institute), Dr. Janet Kerwin (Institute of Genetic Medicine, Newcastle University), and Prof. Cecilia Lo (Department of Developmental Biology, University of Pittsburgh) for generously providing access to human embryo datasets.

CONFLICT OF INTEREST

The author declares no conflict of interest.

AUTHOR'S CONTRIBUTIONS

The author conceived and designed the study, carried out the reconstructions, and wrote the manuscript.

DATA AVAILABILITY STATEMENT

The data that support the findings of this study are available in the supplementary material of this article.

ORCID

Jon Jatsu Azkue https://orcid.org/0000-0002-8609-5500

REFERENCES

AbouHashem, Y., Dayal, M., Savanah, S. & Strkalj, G. (2015) The application of 3D printing in anatomy education. *Medical Education Online*, 20, 29847.

Blaas, H.G., Eik-Nes, S.H., Berg, S. & Torp, H. (1998) In-vivo three-dimensional ultrasound reconstructions of embryos and early fetuses. *Lancet*, 352, 1182–1186.

Born, G. (1883) *Die Plattenmodelliermethode. Archiv für Mikroskopische Anatomie*, 22, 584–599.

Cai, B., Kanagasuntheram, R., Bay, B.H., Lee, J. & Yen, C.-C. (2019) The effects of a functional three-dimensional (3D) printed knee joint simulator in improving anatomical spatial knowledge. *Anatomical Science Education*, 12, 610–618.

Carlson, B.M. (2002) Embryology in the medical curriculum. *Anatomical Record*, 269, 89–98.

Costello, J.P., Olivieri, L.J., Krieger, A., Thabit, O., Marshall, M.B., Yoo, S.-J. et al. (2014) Utilizing three-dimensional printing technology to assess the feasibility of high-fidelity synthetic ventricular septal defect models for simulation in medical education. *World Journal for Pediatric and Congenital Heart Surgery*, 5, 421–426.

de Bakker, B.S., de Jong, K.H., Hagoort, J., de Bree, K., Besselink, C.T., de Kanter, F.E.C. et al. (2016) An interactive three-dimensional digital atlas and quantitative database of human development. *Science*, 354, aag0053.

Dhanantwari, P., Lee, E., Krishnan, A., Samtani, R., Yamada, S., Anderson, S. et al. (2009) Human cardiac development in the first trimester: a high-resolution magnetic resonance imaging and episcopic fluorescence image capture atlas. *Circulation*, 120, 343–351.

Drake, R.L., Lowrie, D.J. Jr & Prewitt, C.M. (2002) Survey of gross anatomy, microscopic anatomy, neuroscience, and embryology courses in medical school curricula in the United States. *Anatomical Record*, 269, 118–122.

Fraser, B.A. & Sato, A.G. (1989) Morphological sex differentiation in the human embryo: a light and scanning electron microscopic study. *Journal of Anatomy*, 165, 61–74.

Geyer, S.H., Mohun, T.J. & Weninger, W.J. (2009) Visualizing vertebrate embryos with episcopic 3D imaging techniques. *Scientific World Journal*, 9, 1423–1437.

Harkness, L.M. & Baird, D.T. (1997) Morphological and molecular characteristics of living human fetuses between Carnegie stages 7 and 23: developmental stages in the post-implantation embryo. *Human Reproduction Update*, 3, 3–23.

Heard, O.O. (1951) Section compression photographically rectified. *Anatomical Record*, 109, 745–755.

Heard, O.O. (1953) The influence of surface forces in microtomy. *Anatomical Record*, 117, 725–739.

Hendrix, M.J., Brailey, J.L. & Shenker, L. (1985) SEM-dissection of a human embryo derived from an ectopic pregnancy. *Early Human Development*, 11, 61–68.

His, W. (1882) *Anatomie menschlicher Embryonen: II Gestalt und Grössenentwicklung menschlicher Embryonen bis zum Schluss des 2. Monats*. Leipzig: Vogel.

Jarvis, D., Griffiths, P.D. & Majewski, C. (2016) Demonstration of normal and abnormal fetal brains using 3D printing from in utero MR imaging data. *American Journal of Neuroradiology*, 37, 1757–1761.

Kass, M., Witkin, A. & Terzopoulos, D. (1988) Snakes: active contour models. *International Journal of Computer Vision*, 1, 321–331.

Kerwin, J., Yang, Y., Merchan, P., Sarma, S., Thompson, J., Wang, X. et al. (2010) The HUDSEN atlas: a three-dimensional (3D) spatial framework for studying gene expression in the developing human brain. *Journal of Anatomy*, 217, 289–299.

Kluth, D., Tenbrinck, R., von Ekesparre, M., Kangah, R., Reich, P., Brandsma, A. et al. (1993) The natural history of congenital diaphragmatic hernia and pulmonary hypoplasia in the embryo. *Journal of Pediatric Surgery*, 28, 456–62. discussion 462–3.

Lim, K.H.A., Loo, Z.Y., Goldie, S.J., Adams, J.W. & McMenamin, P.G.. (2016) Use of 3D printed models in medical education: a randomised control trial comparing 3D prints vs cadaveric material for learning external cardiac anatomy. *Anatomical Sciences Education*, 9, 213–221.

Lorensen, W.E. & Cline, H.E. (1987) Marching cubes: a high resolution 3D surface construction algorithm. *ACM SIGGRAPH Computer Graphics*, 21, 163–169.

Ludwig, K.S. & Landmann, L. (2005) Early development of the human mesonephros. *Anatomy and Embryology*, 209, 439–447.

Mall, F.P. (1914) On stages in the development of human embryos from 2 to 25 mm long. *Anatomischer Anzeiger*, 46, 78–84.

Männer, J., Seidl, W. & Steding, G. (1997) The formal pathogenesis of isolated common carotid or innominate arteries: the concept of malseptation of the aortic sac. *Anatomy and Embryology*, 196, 435–445.

Marsh, K.R., Giffin, B.F. & Lowrie, D.J. Jr (2008) Medical student retention of embryonic development: impact of the dimensions added by multimedia tutorials. *Anatomical Science Education*, 1, 252–257.

McMenamin, P.G., Quayle, M.R., McHenry, C.R. & Adams, J.W. (2014) The production of anatomical teaching resources using three-dimensional (3D) printing technology. *Anatomical Science Education*, 7, 479–486.

Müller, F. & O'Rahilly, R. (1980) The early development of the nervous system in staged insectivore and primate embryos. *Journal of Comparative Neurology*, 193, 741–751.

Müller, F. & O'Rahilly, R. (1987) The development of the human brain, the closure of the caudal neuropore, and the beginning of secondary neurulation at stage 12. *Anatomy and Embryology (Berl)*, 176, 413–430.

Müller, F. & O'Rahilly, R. (1988) The first appearance of the future cerebral hemispheres in the human embryo at stage 14. *Anatomy and Embryology*, 177, 495–511.

O'Rahilly, R. (1979) Early human development and the chief sources of information on staged human embryos. *European Journal of Obstetrics & Gynecology and Reproductive Biology*, 9, 273–280.

O'Rahilly, R. & Müller, F. (1984) Embryonic length and cerebral landmarks in staged human embryos. *Anatomical Record*, 209, 265–271.

O'Rahilly, R. & Müller, F. (1984) Chevalier Jackson lecture. Respiratory and alimentary relations in staged human embryos. New embryological data and congenital anomalies. *Annals of Otology, Rhinology, and Laryngology*, 93, 421–429.

O'Rahilly, R. & Müller, F. (1987) *Developmental stages in human embryos, including a revision of Streeter's 'horizons' and a survey of the Carnegie collection*. Washington: Carnegie Institution of Washington.

O'Rahilly, R. & Müller, F. (1994) *The embryonic human brain. An atlas of developmental stages*. New York: Wiley-Liss.

O'Rahilly, R. & Müller, F. (2010) Developmental stages in human embryos: revised and new measurements. *Cells Tissues Organs*, 192, 73–84.

Olivier, G. & Pineau, M. (1961) "Horizons de Streeter" et âge embryonnaire. *Bulletin de l'Association des anatomistes*, 47, 573–576.

Parisi, F., Rousian, M., Koning, A.H.J., Willemsen, S.P., Steegers, E.A.P. & Steegers-Theunissen, R.P.M. (2019) Effect of human embryonic morphological development on fetal growth parameters: the Rotterdam Periconceptional Cohort (Predict Study). *Reproductive Biomedicine Online*, 38, 613–620.

Pichat, J., Iglesias, J.E., Yousry, T., Ourselin, S. & Modat, M. (2018) A survey of methods for 3D histology reconstruction. *Medical Image Analysis*, 46, 73–105.

Sorkine, O., Lipman, Y., Cohen-Or, D., Alexa, M., Rössl, C. & Seidel, H.-P. (2004) Laplacian surface editing. In: Scopigno, R., Zorin, D., Fellner, D.W. & Spencer, S.N. (Eds.) *SGP '04: Proceedings of the 2004 Eurographics/ACM SIGGRAPH symposium on geometry processing*. New York: Association for Computing Machinery, pp. 179 – 188.

Steding, G. (2008) *The anatomy of the human embryo - a scanning electron-microscopic atlas*. Basel: Karger.

Streeter, G.L. (1951) Developmental horizons in human embryos. Description of age groups XIX, XX, XXI, XXII, and XXIII, being the fifth issue of a survey of the Carnegie Collection (prepared for publication by C. H. Heuser and G. W. Corner). *Contributions to Embryology*, 34, 165–196.

Tait, K., Poyade, M. & Clancy, J.A. (2020) eLearning and embryology: designing an application to improve 3D comprehension of embryological structures. *Advances in Experimental Medicine and Biology*, 1262, 19–38.

Toh, H. & Ohmori, T. (1991) Morphological studies of the foramen caecum linguae of the human and guinea pig tongue. *Acta Anatomica*, 141, 97–103.

Turner, C.L. (1920) A wax model of a presomite human embryo. *Anatomical Record*, 19, 372–412.

Verwoerd-Dikkeboom, C.M., Koning, A.H., van der Spek, P.J., Exalto, N. & Steegers, E.A. (2008) Embryonic staging using a 3D virtual reality system. *Human Reproduction*, 23, 1479–1484.

Weninger, W.J., Geyer, S.H., Mohun, T.J., Rasskin-Gutman, D., Matsui, T., Ribeiro, I. et al. (2006) High-resolution episcopic microscopy: a rapid technique for high detailed 3D analysis of gene activity in the context of tissue architecture and morphology. *Anatomy and Embryology*, 211, 213–221.

World Health Organization (2008) *World health statistics 2008*. Geneva: World Health Organization.

Yamada, S., Itoh, H., Uwabe, C., Fujihara, S., Nishibori, C., Wada, M. et al. (2007) Computerized three-dimensional analysis of the heart and great vessels in normal and holoprosencephalic human embryos. *Anatomical Record*, 290, 259–267.

Yamada, S., Nakano, S., Makishima, H. & Motoki, T. (2018) Novel imaging modalities for human embryology and applications in education. *Anatomical Record*, 301, 1004–1011.

Yamada, S., Samtani, R.R., Lee, E.S., Lockett, E., Uwabe, C., Shiota, K. et al. (2010) Developmental atlas of the early first trimester human embryo. *Developmental Dynamics*, 239, 1585–1595.

Yamada, S., Uwabe, C., Nakatsu-Komatsu, T., Minekura, Y., Iwakura, M., Motoki, T. et al. (2006) Graphic and movie illustrations of human prenatal development and their application to embryological education based on the human embryo specimens in the Kyoto collection. *Developmental Dynamics*, 235, 468–477.

Yammine, K. & Violato, C. (2015) A meta-analysis of the educational effectiveness of three-dimensional visualization technologies in teaching anatomy. *Anatomical Science Education*, 8, 525–538.

Ye, Z., Dun, A., Jiang, H., Nie, C., Zhao, S., Wang, T. et al. (2020) The role of 3D printed models in the teaching of human anatomy: a systematic review and meta-analysis. *BMC Medical Education*, 20, 335.

Young, J.C., Quayle, M.R., Adams, J.W., Bertram, J.F. & McMenamin, P.G. (2019) Three-dimensional printing of archived human fetal material for teaching purposes. *Anatomical Science Education*, 12, 90–96.

Yushkevich, P.A., Piven, J., Hazlett, H.C., Smith, R.G., Ho, S., Gee, J.C. et al. (2006) User-guided 3D active contour segmentation of anatomical structures: significantly improved efficiency and reliability. *NeuroImage*, 31, 1116–1128.

Zilverschoon, M., Kotte, E.M.G., van Esch, B., Cate, O.T., Custers, E.J. & Bleys, R.L. (2019) Comparing the critical features of e-applications for three-dimensional anatomy education. *Annals of Anatomy*, 222, 28–39.

SUPPORTING INFORMATION

Additional supporting information may be found online in the Supporting Information section.

How to cite this article: Azkue, J.J. (2021) External surface anatomy of the postfolding human embryo: Computer-aided, three-dimensional reconstruction of printable digital specimens. *Journal of Anatomy*, 239, 1438–1451. https://doi.org/10.1111/joa.13514